Potential of Synthetic Aperture Radar Sentinel-1 time series for the monitoring of phenological cycles in a deciduous forest

Kamel Soudani[1], Nicolas Delpierre[1,2], Daniel Berveiller[1], Gabriel Hmimina[3], Gaëlle Vincent[1], Alexandre Morfin[1], Éric Dufrêne[1]

[1] Université Paris-Saclay, CNRS, AgroParisTech, Ecologie Systématique et Evolution, 91405, Orsay, France.

[2] Institut Universitaire de France (IUF).

[3] Laboratoire de Météorologie Dynamique, IPSL, CNRS/UPMC, Paris, France.

* Correspondence: kamel.soudani@universite-paris-saclay.fr

Abstract:

Annual time-series of the two satellites C-band SAR (Synthetic Aperture Radar) Sentinel-1 A and B data over five years were used to characterize the phenological cycle of a temperate deciduous forest. Six phenological markers of the start, middle and end of budburst and leaf expansion stage in spring and the leaf senescence in autumn were extracted from time-series of the ratio (VV/VH) of backscattering at co-polarization VV (vertical-vertical) and at cross polarization VH (vertical-horizontal). These markers were compared to field phenological observations, and to phenological dates derived from various proxies (Normalized Difference Vegetation Index NDVI time-series from Sentinel-2 A and B images, *in situ* NDVI measurements, Leaf Area Index LAI and litterfall temporal dynamics). We observe a decrease in the backscattering coefficient (σ^0) at VH cross polarization during the leaf development and expansion phase in spring and an increase during the senescence phase, contrary to what is usually observed on various types of crops. In vertical polarization, σ^0VV shows very little variation throughout the year. S-1 time series of VV/VH ratio provides a good description of the seasonal vegetation cycle allowing the estimation of spring and autumn phenological markers. Estimates provided by VV/VH of budburst dates differ by approximately 8 days on average from phenological observations. During senescence phase, estimates are positively

29   shifted (later) and deviate by about 20 days from phenological observations of leaf senescence

30   while the differences are of the order of 2 to 4 days between the phenological observations and

31   estimates based on *in situ* NDVI and LAI time-series, respectively. A deviation of about 7 days,

32   comparable to that observed during budburst, is obtained between the estimates of senescence

33   from S-1 and those determined from the in situ monitoring of litterfall. While in spring, leaf

34   emergence and expansion described by LAI or NDVI explains the increase of VV/VH (or the

35   decrease of σ^0VH), during senescence, S-1 VV/VH is decorrelated from LAI or NDVI and is

36   better explained by litterfall temporal dynamics. This behavior resulted in a hysteresis

37   phenomenon observed on the relationships between VV/VH and NDVI or LAI. For the same

38   LAI or NDVI, the response of VV/VH is different depending on the phenological phase

39   considered. This study shows the high potential offered by Sentinel-1 SAR C-band time series

40   for the detection of forest phenology for the first time, thus overcoming the limitations caused

41   by cloud cover in optical remote sensing of vegetation phenology.

42

43   **Keywords**: Phenology; Forest, Sentinel 1; VV/VH; NDVI; LAI

44   **Highlights**:

45   • We study S-1 C-band dual polarized data potential to predict forest phenology

46   • Seasonal phenological transitions were accurately described by S-1 time-series

47   • Budburst and senescence dates from S-1 differ from direct observations by one week

48   • Time-series of S-1 VV/VH, NDVI, LAI and litterfall were also compared

49   • Relationships VV/VH vs NDVI and LAI show a hysteresis according to the season

50

51   **1. Introduction**

52   In forest ecosystems, the opening of buds ("budburst") in spring and the coloration and fall

53   of leaves ("leaf senescence") mark the start and the end of the photosynthetically active period

54   and therefore play a key role in their productivity and carbon storage activity (Richardson et al.,

55   2010). Historically, the timings of these phenological events have been monitored through

56   direct and periodic human observations of trees in the field. However, this method is

57   time-consuming, laborious, non-standardized and subject to an observer effect (Schaber and

58   Badeck, 2002). Alternative indirect field techniques (RGB camera, proximal remote sensing

59   systems, micrometeorological radiation sensors, etc.) are also used to monitor the seasonal

60   cycle of forest canopy (Soudani et al., 2020). However, phenological metrics derived from both

61   direct field observations and indirect proximal techniques are spatially spare and fail to describe

62   the spatial and temporal variability in phenology due to the vegetation and micro-climate

63   diversity (Soudani et al., 2012). Field observations also target a limited set of species and may

64   not always be representative at the ecosystem scale. Satellite based remote sensing, because of

65   its great potential for spatial sampling, constitutes the main approach for estimating and

66   mapping phenological metrics at local to regional scales (Reed et al., 2003). However, the

67   assessment of this potential has been severely limited by the difficulty of linking

68   satellite-derived phenological metrics to field phenological observations, mainly due to

69   temporal and spatial scale mismatches (Fisher et al., 2006). A few years ago, constellations of

70   identical satellites such as SPOT 6/7, Pleiades, and more particularly, Sentinel-2 A and B in the

71   optical domain and Sentinel-1 A and B in the C-band microwave frequency (5.405 GHz, 5.6

72   cm) have been launched, with the aim of overcoming these scale-related limitations by allowing

73   image acquisitions with both good temporal and spatial resolutions under the same viewing

74   angles (Ose et al., 2016). S2-A and S2-B, launched in 2015 and in 2017, that occupy the same

75   orbit but 180° apart from each other, provide a temporal resolution of 10 days each and around

76   5 days with S2-A and S2-B together, reduced to 2-3 days over mid-latitudes regions. Spatial

77   resolution of S2 varies from 10 m to 60 m depending on the spectral band. SAR (Synthetic

78   Aperture Radar) S-1A and S-1B, launched in 2015 and 2016 respectively, together offer a

79   temporal resolution about 3 days at the equator, > 1 day at high latitude and about 2 days in

80   Europe combining ascending and descending orbits at a spatial resolution of 10 m in

81   Interferometric mode (ESA, Sentinel-1 user guide). Temporal resolution of S-2 and S-1 are

82   therefore comparable to the occurrence of phenological observations collected in the field over

83   forest ecosystems, usually once or twice a week, and the spatial resolutions of 10 m and 20 m

84   are also comparable to the size of adult forest tree crowns.

85   Typically, vegetation phenological metrics are derived from the analysis of time-series of

86   spectral vegetation indices (SVI) in the optical domain but SVI are subject to varying degrees of

87   uncertainty due mainly to cloud cover and cloud shadow contamination, which either

88   introduces random noise that is difficult to correct or makes the data totally unavailable (Hird

89   and McDermid, 2009; White and Wulder, 2013). Therefore, the temporal resolution of the

90   satellite-based optical sensors is nominal since the availability of data depends on sky

91   conditions (Wang and Atkinson, 2018; Sudmanns et al., 2019). In comparison to optical remote

92   sensing, the main advantage of SAR remote sensing is its ability to pass through clouds with

93   negligible attenuation. Temporal resolution is therefore maintained from year to year or from

94   one region to another regardless of cloud conditions.

95   While the potential of S-2 for estimating forest phenology has been evaluated in many

96   studies (Lange et al., 2017; Vrieling et al., 2018; Kowalski et al., 2020; Bolton et al., 2020),

97   little is known about the potential of SAR data in general and S-1 in particular. The potential of

98   S-1 has previously been assessed to monitor phenology, productivity and cultural practices in

99   crops and meadows (Vavlas et al., 2020; Song and Wang, 2019; Stendardi et al., 2019), but at

100   the exception of the study by Rüetschi et al. (2018), to the best of our knowledge no other

101   studies which have compared phenological estimates derived from S-1 with field phenological

102   observations in deciduous forests. In Rüetschi et al. (2018), few field phenological observations

103   were available and, as pointed out by the authors, the temporal resolution of used S-1

104   time-series (24 days) was not adequate for an accurate assessment. In another studies,

105   Dostálová et al. (2016; 2018) and Frison et al. (2018) analyzed time-series of S-1 over

106   deciduous and coniferous forest stands. However, these studies were limited to the analysis of

107   the temporal patterns of the S-1 data and did not focus on their exploitation for the detection of

108   phenological dates.

109   In this paper, our first objective is to investigate the potential of time series of S-1 A&B

110   C-band dual-polarized (VV and VH) SAR images to describe the phenological patterns of a

111   temperate deciduous forest, and to estimate the timings of the main spring and autumn

112   phenological stages. To this aim, we compared S1-based spring and autumn phenological

113   estimates to in situ phenological observations by human observers and to estimates from

114   alternative in situ indirect approaches including daily time-series of proximal NDVI

115   (normalized difference vegetation index), daily time-series of LAI (Leaf Area Index) estimated

116   from continuous radiation measurements and time-series of NDVI derived from S-2 A&B

117   images. During the autumnal phenological stage, we also compared S1-based phenological

118   dates to temporal dynamics of litterfall monitored in the field. Finally, and as a secondary

119   objective of this paper, we further analyzed the sudden and abrupt changes observed in

120   backscattering coefficients in the light of continuous measurements of precipitation and soil

121   water content at different depths.

122

123   **2.   Materials and Methods**

124   2.1. Site description

125   The study site is the Fontainebleau-Barbeau forest station (48°28'26"N, 2°46'57"E),

126   located 53 km southeast of Paris (Supplementary Figure S1). Briefly, Fontainebleau-Barbeau

127   forest is mainly composed of sessile oak (*Quercus petraea* (Matt.) Liebl), with an understory of

128   hornbeam (*Carpinus betulus* L.). The stand age is about 150 years and the dominant height is 27

129   m. The topography is flat, and the ground elevation is about 103 m a.s.l. On this site which

130   belongs to the pan-European ICOS Ecosystem network (Integrated Carbon Observation

131   System, ICOS code FR-Fon), a 35-m high tower has been installed in 2005, measuring energy

132   and matter (CO_2 and H_2O) exchanges between the vegetation and the atmosphere using the

133   eddy-covariance technique. More details can be found in Delpierre et al. (2016) and at

134   http://www.barbeau.u-psud.fr/index-fr.html.

135

136   2.2. Data

137   2.2.1. SAR Sentinel-1 C-band time-series

138   Time-series of SAR Sentinel-1 (A&B) backscattering coefficient (σ^0) at VH and VV

139   polarization were composed using the Google earth engine (GEE) cloud. A total of 470 dual

140   polarized (VV and VH) images covering the period from 01/01/2015 to 31/12/2019 were used.

141   225 scenes are in ascending orbit and 245 in descending orbits. Before September 2016 (day of

142   year 278), S-1 time series are composed of S-1A images only. The number of S-1 images used

143   per year is 43 images in 2015, 74 in 2016, 119 in 2017, 117 in 2018 and 117 in 2019; thus an

144   average of about 1 image every 8 days in 2015, 1 image every 5 days in 2016 and 1 image every

145   3 days in 2017/2018 and 2019. As mentioned above, the number of images available in 2015 is

146   low since only S-1A was operational. Images are in GRD (Ground Range Detected) format, in

147   interferometric wide swath mode (IW), calibrated and ortho-corrected using the Sentinel-1

148   Toolbox at 10-m spatial resolution. Viewing incidence angle is about 39.30°. Each image

149   contains two layers of the backscattering coefficient σ_0 in VV and VH dual polarization

150   converted in decibels unit (dB). Time-series of σ_0 were composed based on their means within a

151   circular buffer of 50 m in radius, centered on the Fontainebleau-Barbeau flux tower (Fig. S1).

152   The number of S-1 pixels within the buffer is about 78 pixels. To remove noise, time series of

153   VV/VH ratio in dB unit, calculated as (σ^0VV (dB) - σ^0VH (dB)), were filtered using the

154   Savitzky-Golay filtering method under the MATLAB software. The best filtering was obtained

155   with the following parameters: 2nd polynomial order and 5 or 9 window length.

156

157   2.2.2. Sentinel 2 A & 2B time-series

158   A total of 284 Sentinel-2 (A&B) images (193 S-2A and 91 S-2B) from the S-2 L1-C TOA

159   reflectance product were processed under GEE to generate NDVI time series using bands 4

160   (red) and 8 (near infrared) over the period 2015-2019. The corresponding wavelengths are

161   respectively 664.5 nm (S-2A) / 665 nm (S-2B) for the red band and 835.1 nm (S-2A) / 833 nm

162   (S-2B) for the near infrared band. The NDVI was calculated per pixel and averaged over the

163   same 50 m diameter buffer as for S-1 A&B. The spatial resolution of the S-2 red and near

164   infrared bands is 10 m and the number of pixels within the circular buffer is the same as for S-1

165   (78 pixels). Pre-filtering of cloudy pixels was performed using the QA60 flag, bits 10 and 11,

166   which provide information about clouds and cirrus at the 60 m pixel scale. Only cloudy and

167   cirrus-free pixels within the buffer were used in the calculation of NDVI. The number of S-2

168   images per year is 4 images in 2015, 11 in 2016, 17 in 2017, 28 in 2018 and 31 in 2019. From

169   June 2015 to March 2017, only S-2A was operational, explaining the low number of images

170   available for these two years. The year 2015 was excluded from the analysis due to the

171   insufficient number of images.

172

173   2.2.3 In situ data

174   2.2.3.1. Field phenological observations

175   A description of field phenological data is given in Denéchère et al. (2019), Delpierre et al.

176   (2020) and Soudani et al. (2020). Briefly, phenological observations were conducted according

177   to two complementary sampling protocols. The first protocol (hereafter *intensive*) protocol was

178   conducted from 2015 to 2017 for both spring and autumn. In this protocol, temporal dynamics

179   of spring (percentage of open buds) and autumn (percentage of colored and/or fallen leaves)

180   phenological transitions were determined at tree level, on 30 to 66 trees from the early signs to

181   the end of each phenological stage. The second protocol (hereafter *extensive*) protocol was

182   conducted on 2018 and 2019, during the spring phase only. In this protocol, we determined the

183   date of budburst visually at the whole plot level surrounding the flux tower on about 100 trees.

184   We considered that a tree had reached budburst when 50% of its crown showed open buds.

185   Budburst of the whole plot was reached when 50% of sampled trees have reached budburst. All

186   observations were achieved using binoculars, on a bi-weekly basis during the budburst

187   (BB-OBS) and weekly during the senescence (LS-OBS). Hence the uncertainties are 3.5 days

188   for BB-OBS and 7 days for LS-OBS.

189

190   2.2.3.2. Narrow-band NDVI data

191   The NDVI is calculated as follows: $NDVI = (NIR - R)/(NIR + R)$. R and NIR are

192   radiances in the red and the near infrared bands, respectively. Radiances are measured using a

193   laboratory made NDVI sensor. A description of this sensor and its use for estimating

194   phenological metrics in various biomes is given in Soudani et al. (2012; 2020) and Hmimina et

195   al. (2013). Briefly, the sensor is positioned at the top of the flux tower in the

196   Fontainebleau-Barbeau forest, about 7 m above the canopy, pointing downwards and inclined

197 about 20-30° from vertical and facing south to avoid the hot-spot effects in canopy reflectance

198 when the viewing direction is collinear with the solar direction. The field of view of the sensor

199 is 100° and the observed area is a few tens of m². Measurements are acquired continuously

200 every half-hour. Noisy data, due mainly to rainfall and very low radiation conditions, were

201 removed according to the procedure described in Soudani et al. (2012). Daily average of filtered

202 NDVI data acquired between 10h and 14h (UT) is considered to minimize daily variations in

203 solar angle.

204

205   2.2.3.3. Leaf Area Index LAI

206   For the different years, the maximum of leaf area index reached during the summer is

207 determined directly using the litter collection method. 20 litter traps of 0.5 m^2 each were used

208 according to the standard protocol adopted within the framework of the European ICOS

209 Ecosystem network (Gielen et al. 2018). The litter collection during the autumn is carried out at

210 a one-week time step, thus allowing, in addition to the determination of maximum LAI, the

211 description of temporal dynamics of surface area of fallen leaves from the first fallen leaves

212 until the end of the autumn season.

213   Continuous estimation of canopy LAI was also achieved by applying the Beer-Lambert

214 law to continuous measurements of incoming and beneath canopy radiation in the PAR

215 (Photosynthetically active radiation) spectral range at a half-hourly time step. Beneath canopy

216 radiation is measured using 15 sensors, installed on the ground-area surrounding the flux tower

217 to ensure a robust spatial sampling of the radiation transmitted through the canopy. Since the

218 application of BL's law requires the prior determination of the extinction coefficient K, the

219 latter was estimated from average LAI maximum determined from the litter collection method

220 and average transmitted PAR during the summer growing season. To describe the temporal

221 dynamics of LAI, this coefficient was assumed to be constant throughout the year. More details

222 about the LAI calculation from radiation measurements are given in Soudani et al. (2020).

223

224   2.2.3.4. Precipitations and soil moisture content

225 Rainfall and soil water content were measured at a half-hourly resolution. Rainfall is

226 automatically measured using a rain gauge installed at the top of the tower (Model R01 3029,

227 PRECIS MECANIQUE SAS, France). Soil water content is automatically measured every half

228 hour and every 10 cm from the topsoil to 150 cm below the soil surface using 4 probes installed

229 in the vicinity of the tower (SENTEK, Enviroscan system).

230

231 2.3. Methods

232 2.3.1. Extraction of phenological metrics in spring and autumn from time-series

233 Six phenological metrics were extracted from daily time-series of S-1 VV/VH, in situ

234 NDVI, S-2 NDVI, LAI and field phenological observations collected according to the intensive

235 protocol. Three phenological metrics were also extracted from litterfall temporal dynamics.

236 The extraction is carried out according to Soudani et al. (2008). Briefly an asymmetric double

237 sigmoidal function (ADS) was fitted to time-series according to the following equation:

$$Vv(t) = (w_1 + w_2) + \frac{1}{2}(w_1 - w_2)[\tanh(w_3(t-u)) - \tanh(w_4(t-v))]$$

238 Vv (t) is the considered vegetation variable (VV/VH, NDVI from S-2 and in situ measurements,

239 LAI, % of open buds, % of colored and/or fallen leaves). t is the time (day of year). tanh is the

240 hyperbolic tangent and w_1, w_2, w_3, w_4, u, v are the fitted parameters. (w_1+w_2) is the Vv minimum

241 in unleafy season. (w_1-w_2) is the total amplitude of the Vv seasonal cycle. The six phenological

242 markers are named as follows: SOS, MOS and EOS for the start, middle, and end of season in

243 spring and SOF, MOF and EOF for the start, middle and end of season in autumn, according

244 Klosterman et al. (2014). The parameters were fitted by minimizing the sum of squares of

245 differences between predicted and measured Vv. To constrain the fit at the end of the growing

246 season, each year of VV/VH, NDVI and LAI data was extended to the winter of the following

247 year. All dates were determined using the ADS function fitted to the data, except for SOF and

248 EOF dates determined from litterfall temporal dynamics. For litterfall time-series, MOF is

249 determined using the ADS function but SOF and EOF are determined directly from the data,

250 due to the poor quality of the fit on both sides of ADS function. SOF and EOF are, respectively

251 the dates corresponding to 10% and 90% of the total litterfall.

9

252

253   2.3.2. Statistical analysis

254   The performance of VV/VH time-series to predict phenological events in spring and

255   autumn was evaluated with respect to the field phenological observations using the mean bias

256   error (MBE) and the mean absolute deviation (MAD) between estimated (P_i) and observed

257   dates (O_i) for the different years (N), calculated as follows:

258
$$MBE = \frac{1}{N}\sum_{i=1}^{N}(P_i - O_i)$$

$$MAD = \frac{1}{N}\sum_{i=1}^{N}|(P_i - O_i|$$

259   Statistical significance is determined at 5% probability level using one-tailed and two-tailed

260   Student's t-test for comparison of means. When linear regressions between different variables

261   are investigated, R^2 is used to assess the strength of these relationships. Statistical analysis was

262   done using the R software.

263

264   **3. Results**

265   3.1. SAR Sentinel-1 VV/VH time-series

266   S-1 VV/VH time-series are shown in Figure 1. σ^0 in VV and VH polarization in ascending

267   and descending orbits are shown in Figure S2, in supplementary material. Using S-1 original

268   data (before filtering, Figure S2 for more details), the coefficient of backscattering σ^0 is on

269   average, over all years, about -8.54 dB ([-10.73 , -5.07]) in VV polarization and about -14.40

270   dB ([-17.48 , -10.45]) in VH. The difference between the two polarization is very highly

271   significant (P < 0.001). Considering both ascending and descending orbits, differences in

272   means are about 0.5 dB in both polarizations but are statistically significant. However,

273   differences between means are not significant for VV/VH (P < 0.34). For this reason, S-1 data

274   acquired at the two orbits are considered without distinction in the following.

275   On the other hand, the analysis of the temporal dynamics of σ^0VH and σ^0VV shows

276   intermittent sudden and abrupt changes. Weak relationships are observed between σ^0VV,

277   σ^0VH, VV/VH and soil moisture between 0-10 cm over the year (R^2 0.07; 0.26 and 0.148,

278   respectively) but these relationships disappear when separating the summer leafy and winter

10

279   unleafy seasons in the analysis (Figures S3 & S4). During the summer period, although weak, a

280   significant positive relationship was obtained between rainfall and $\sigma^0 VH$ (R² = 0.124, P <

281   0.008).
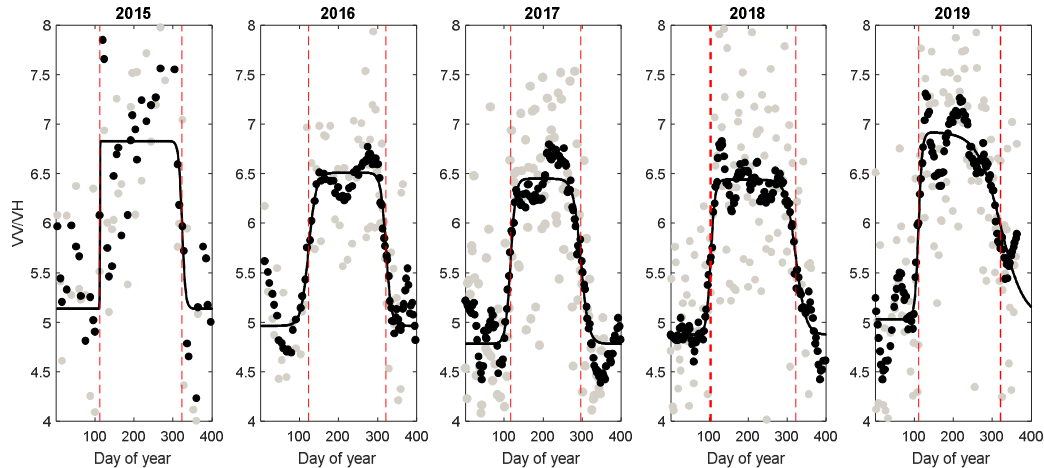
282

283   Figure 1: Sentinel-1 VV/VH time-series (dB): grey circle: original data; black circle: data
284   smoothed using a Savitzky-Golay filter; continuous black curve: asymmetric double sigmoid
285   function (ADS) fitted to VV/VH smoothed data. Red vertical bars: estimated phenological
286   transition (MOS and MOF) dates from VV/VH time-series based on ADS function.

287

288   Figure 1 shows that S-1 VV/VH temporal patterns reproduce the forest phenology

289   observed in deciduous forests with good accuracy. Four phases can be distinguished: a winter

290   phase with low VV/VH values, a rapid transition phase during spring when VV/VH increases

291   quickly, a plateau during the main growing season in summer and a fourth phase of VV/VH

292   decline which coincides with the phase of leaf senescence and leaf fall. In comparison with the

293   backscattering coefficients $\sigma^0 VH$ or $\sigma^0 VV$, the VV/VH ratio is more dynamic and seems to be

294   driven by VH more than VV polarization (Figure S2).

295   Indeed, the backscatter coefficient $\sigma^0 VH$ decreases during spring phenological transitions,

296   and remains relatively stable during the summer for which LAI remains stable and increases

297   again during autumn phenological transitions (Figure S2). Between its winter maximum and

298   summer minimum, $\sigma^0 VH$ varies on average from -13.36 dB (standard deviation 0.871 dB) in

299   winter [doy 330-98 next year] to -15.16 dB (standard deviation 0.851 dB) in summer [doy

300   128-270]. The decrease is of 1.80 dB, but $\sigma^0 VH$ is highly significantly lower in summer than in

301   winter (P <0.001, one-sided t-test). In vertical polarization, $\sigma^0 VV$ decreases from -8.43 dB

11

302   (0.732 dB) in winter to -8.51 (0.710 dB) in summer (Figure S2). The decrease is only about 0.15

303   dB but is statistically significant at 5% (P <0.048). In the VV/VH, driven by changes in σ^0VH,

304   the average increases from 4.93 dB (0.77 dB) in winter to 6.56 dB (0.79 dB) in summer. Also,

305   VV/VH is very significantly higher in summer than in winter (P<0.001, one tailed t-test).

306

307   3.2. Phenological markers derived from SAR Sentinel-1 VV/VH time-series

308   The temporal dynamics of VV/VH strongly co-vary with the canopy phenological cycle, as

309   assessed through various proxies (Figure 2). Summary statistics are given in Table 1 and

310   estimated dates by year and for the six phenological metrics (SOS, MOS, EOS in spring and

311   SOF, MOF and EOF in autumn) are given in Supplementary Material S5.
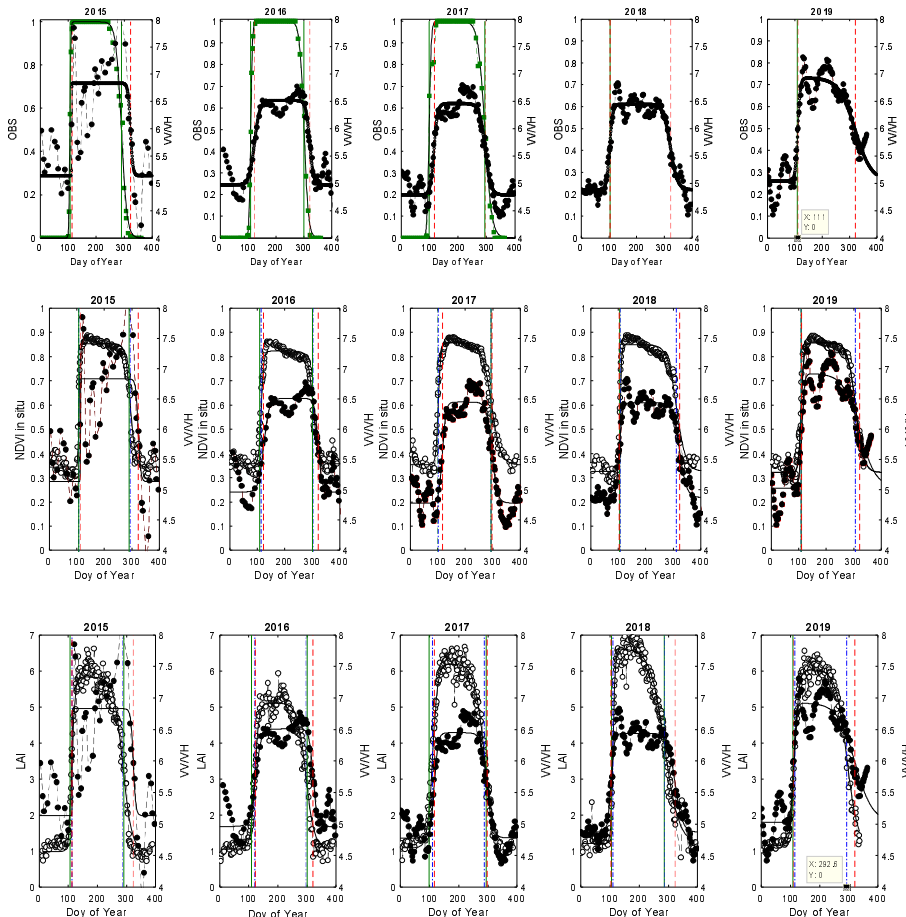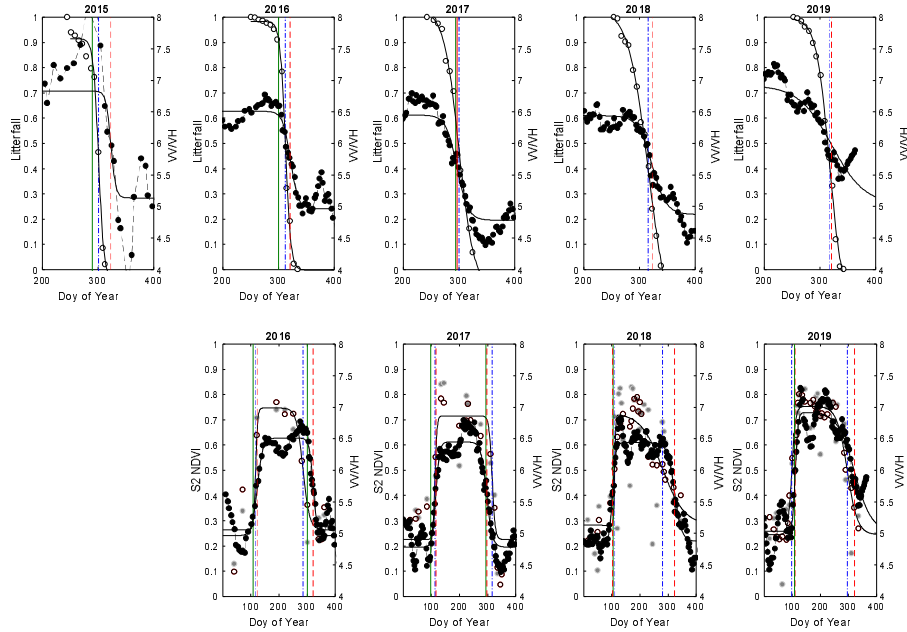
Figure 2: Sentinel-1 VV/VH time-series for all subplots (black filled circles – right axis). Empty circles – left axis: from top to bottom – time-series of field phenological observations (OBS from intensive protocol on 2015-2017), ground-based NDVI, Leaf Area Index (LAI), Litterfall in autumn and Sentinel 2 NDVI. Vertical bars: observed phenological transition dates in green (OBS from intensive and extensive protocols); estimated MOS and MOF phenological transition dates based on ADS function using VV/VH time-series in red and predicted phenological dates from in situ NDVI, LAI, S-2 NDVI (gray circle – removed using SG filter; empty circle – used) and litterfall in blue.

	Onset of greenness and leaf expansion			Leaf senescence and fall		
	SOS	MOS	EOS	SOF	MOF	EOF
Phenological observations (*)	97 (89-102)	105.5 (99-109)	110.5 (108-115)	272 (267-282)	294.5 (290-300)	316.5 (321-321)
S-1 VV/VH	100 (89-110)	113.5 (104-123)	124.5 (113-144)	287 (252-312)	317 (297-323)	345 (318-388)
In situ NDVI	98 (90-103)	107.5 (101-113)	115.5 (111-123)	270 (255-280)	301 (293-311)	331.5 (314-349)
S-2 NDVI	102.5 (83-115)	110 (99-118)	119 114-124	252 (192-303)	294 (281-316)	338 (320-368)
LAI	98.5 (90-103)	114 (111-120)	128 (119-137)	248.5 (231-263)	290 (287-296)	330.5 (322-341)
Litterfall	-	-	-	281 (266-298)	309 (300-317)	323 (309-331)

321 Table 1: Summary statistics (mean and min-max) of observed and estimated phenological
322 dates. SOS, MOS and EOS for the start, middle, and end of season in spring and SOF, MOF and
323 EOF for the start, middle and end of season in autumn. (*) For field phenological observations,
324 MOF is determined for the five years from the extensive protocol. SOS, EOS, SOF, MOF and
325 EOF, are determined for years 2015 to 2017 using the intensive protocol.
326
327 　　　Figure 3 illustrates the interannual variations in estimated budburst (MOS) and senescence
328 dates (MOF) for the different approaches.
329
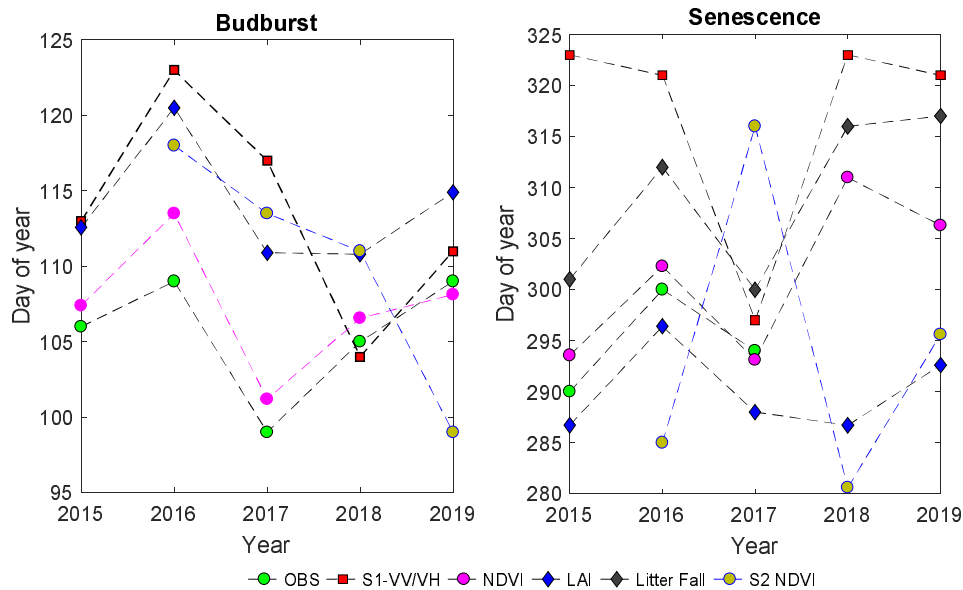
330
331 Figure 3: Average dates of budburst (a- left) and senescence (b- right) based on MOS and MOF,
332 respectively.

333 　　　During the spring transition phenological stage, and based on MOS criterion, VV/VH
334 time-series lag about 8 days behind the observed budburst date (MBE and MAD, 8.5 and 8 days
335 respectively; Figure 3a). This lag with observed budburst dates is similar to the lag of MOS
336 retrieved from LAI time-series (MBE and MAD of about 8.5 days) and is slightly lower by
337 about 1.5 days in comparison to the lag between MOS estimates retrieved from S-2 NDVI
338 time-series (for S-2 NDVI, MBE and MAD of about 10 days and 5 days, respectively). The best
339 estimates are obtained using in situ NDVI time-series for which MBE and MAD are about 2
340 days. During the autumnal phenological phase, for the three years for which continuous field
341 observations are available, VV/VH time-series provide estimates which are approximately 20
342 days later than the observed dates (Figure 3b) while the differences are of the order of 2 to 4

14

343   days between the observations and estimates based on in situ NDVI and LAI, respectively.

344   Interestingly, MOF derived from VV/VH differs by 7 days on average from MOF determined

345   from litterfall time series. Between S-1 and S-2 based estimates, MBE and MAD are

346   respectively of - 4 days (S2-based estimates later) and 7 days during the spring and -20 days

347   (S-2 earlier) and 30 days in autumn (Figure 3b, Table S5).

348   These differences between VV/VH estimates and those obtained using field phenological

349   observations and the other alternatives methods reflect different relationships between the

350   temporal dynamics of the VV/VH signal and canopy properties. Figure 4 illustrates the

351   relationships between VV/VH or LAI and in situ NDVI during four distinct phenological

352   stages: winter dormancy period, spring leaf emergence and expansion stage, summer growth

353   stage, and autumnal leaf senescence and fall. Four years, from 2016 to 2019, for which more S1

354   data are available and phenological estimates are more robust.
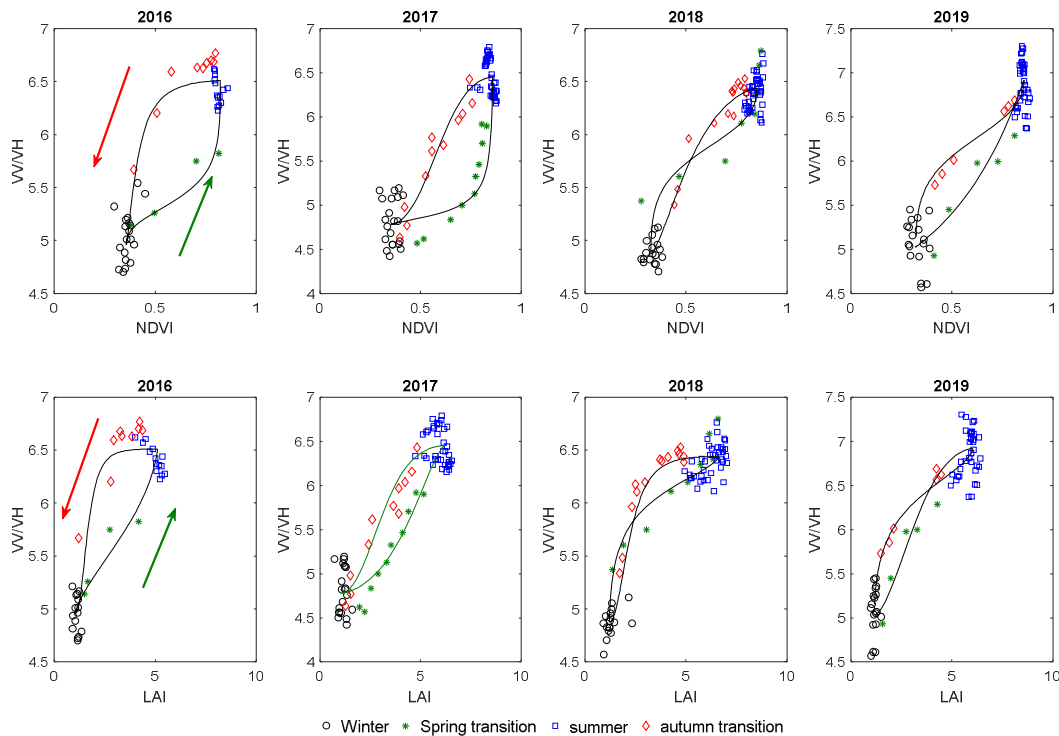
355

356   Figure 4: Relationships between VV/VH (dB) and in situ NDVI (top) and LAI (bottom)
357   according to the phenological stage. Symbols are measurements: winter (day of year: 330-98 of
358   the next year) in black circles; spring transition (day of year 98-128) in green stars; summer
359   growing season (day of year 128-270) in blue square; autumn transition (day of year 270-330)
360   in red diamond. Continuous curves are predicted values using the ASD function. Red and green

361   arrows give the directions of VV/VH trajectories during the autumn (red) and spring (green)

362   phenological stages, respectively.

363

364   Figure 4 shows a positive relationship between VV/VH and both NDVI and LAI. These

365   relationships are not unique and depend on the phenological stage considered. A hysteresis

366   phenomenon can be noted as the VV/VH trajectories are not identical during the increase and

367   the decrease in canopy leaf area as described using LAI or NDVI, during spring and autumn,

368   respectively. For the same NDVI (or LAI), VV/VH is higher during the fall phase than during

369   the spring phase.

370   **4**. **Discussion**

371   Examination of the temporal dynamics of the VV/VH signal shows significant rapid

372   variations that seem to be linked to rainy events (Figure 1, Figures S3 & 4). C-band sensitivity

373   to precipitations intercepted and stored by the canopy during data acquisition has been shown in

374   previous studies from measurements (Benninga et al., 2019; El Hajj et al., 2016; Proisy et al.,

375   2000) and from simulations (Jong et al., 2016). As underlined above, the relationship between

376   S-1 backscattering and soil water content is better in VH than in VV polarization and is only

377   significant when both the unleafy and leafy seasons are combined (Figure S4). Therefore, this

378   relationship seems to be caused more by the changes in canopy properties than by direct

379   influences of soil moisture on backscatter coefficients. As also shown in Figure S3, $\sigma^0 VH$ is

380   more sensitive to the phenological cycle observed in deciduous forests while the temporal

381   profile of $\sigma^0 VV$ remains relatively stable throughout the year. $\sigma^0 VH$ shows an average decrease

382   of about 1.80 dB on average during summer in comparison to winter. This result agrees with the

383   studies of Rüetschi et al. (2018), Dostálová et al. (2016; 2018) and Frison et al. (2018) in which

384   they observe a lower backscattering coefficient in the S-1 VH polarization in summer than in

385   winter in temperate deciduous forests. In Rüetschi et al. (2018), the differences observed on two

386   oak stands and over two consecutive years ranged from 0.38 dB to 1.96 dB in VH polarization.

387   In VV polarization, a lower average in summer than in winter was observed on a single oak

388   stand. The difference was of 0.76 dB, but in general, there is no a well-established seasonal

389   effect on $\sigma^0 VV$ and the sign of the difference between summer and winter $\sigma^0 VV$ varied. $\sigma^0 VV$

16

390   was considered relatively stable throughout the year while σ^0VH responds significantly to the

391   seasonal vegetation cycle. In Rüetschi et al. (2018), the behavior of σ^0VH was also verified over

392   a whole region at the S-1pixel scale. Deciduous stands, composed mainly of oak and beech,

393   showed most often a lower VH backscattering in summer than in winter. An opposite behavior

394   was observed on coniferous stands, composed mainly of spruce, for which the σ^0VH is higher

395   in summer than in winter. Dostálová et al. (2016; 2018) also observed a clear decrease in S-1

396   VH signal during the spring and an increase during the senescence transition stage in the range

397   of 0.5 to 2 dB in broadleaf forests of oak, beech, maple and birch trees. Similar results were

398   obtained by Frison et al. (2018) over the whole Fontainebleau forest massif to which the

399   Fontainebleau-Barbeau forest (our study site) belongs. The authors observed a decrease

400   in σ^0VH in spring from -12.5 to -15 dB, while σ^0VV remains relatively constant.

401   Rüetschi et al. (2018) and Dostálová et al. (2016; 2018) explained the decrease in VH

402   backscatter during the growing season, when leaf biomass is at its maximum, by a lower

403   contribution of branches to backscattering, considered more reflective than leaves in C-band,

404   and by a lower contribution of soil masked by foliage.

405   The sensitivity of σ^0VH and VV/VH to phenology shown in our study (Figures 1 and S3)

406   and in Rüetschi et al. (2018), Dostálová et al. (2016; 2018) and Frison et al. (2018),

407   characterized by a decrease of the former and an increase of the latter during the summer, is

408   different from what can be observed on various types of crops as shown in many studies

409   (Veloso et al., 2017; Khabbazan et al., 2019; Stendardi et al., 2019; Dostálová et al., 2018) in

410   which an increase in σ^0VH signal and a decrease in VV/VH ratio when biomass increases in

411   maize, soybean, sunflower, potatoes crops and in alpine meadows. In those studies, the increase

412   of σ^0VH backscattering was explained by the increase in vegetation volume scattering acting as

413   the main backscatter.

414   As underlined above, VV/VH ratio is more dynamic than σ^0VH and σ^0VV and better

415   describes the seasonal dynamics of the canopy (Figures 1 & S3). VV/VH is also known to be

416   more stable and able to reduce the soil moisture and soil-vegetation interactions effects

417   (Vreugdenhil et al., 2018; Veloso et al., 2017). As shown in Figure 2, S-1 VV/VH reproduces

418   the annual cycle of phenological events observed in deciduous forests with varying degrees of

419   fidelity.

420   The estimated phenological dates using MOS marker from VV/VH time-series are in

421   agreement with the observed dates, with a positive bias of about 8 days during spring (Figure

422   3). A similar bias is obtained using the LAI time series. Indeed, during the spring transition

423   phase (Figure 2), we observe that time-series of VV/VH overlap with those of LAI but deviate

424   very significantly during the fall phase. During this phase, temporal patterns of VV/VH are

425   positively shifted with respect to those of LAI. It can also be noted that temporal patterns of

426   litterfall are also positively shifted in comparison to temporal patterns of LAI estimated from

427   transmitted PAR. The average bias between estimates of the senescence date decreases from

428   about 27 days between VV/VH and LAI to about 7 days between VV/VH and litterfall. During

429   the senescence and compared to *in situ* and S-2 NDVI, VV/VH provides estimates that are

430   generally later, between 4 and 30 days, with an average bias of 17 days compared to *in situ*

431   NDVI and between -19 and 42 days and an average bias of 20 days with S-2 NDVI.

432   While during the spring phase, the patterns of VV/VH, LAI and NDVI from *in situ* and S-2

433   data, are relatively close, they deviate very strongly during the senescence phase causing large

434   differences in the estimation of senescence dates (Figure 2). During this phase, VV/VH decay

435   seems to more closely follow the temporal dynamics of litterfall than the LAI or NDVI decay.

436   These results show that the relationships between VV/VH and LAI or NDVI are not stable but

437   depend on the phenological stage considered. For the same LAI or NDVI, the VV/VH signal is

438   generally weaker during the spring phenological stage than during senescence (Figure 4). This

439   implies that the canopy characteristics that modulate these variables are different. During

440   spring, the concomitance of VV/VH increase with the increase of LAI and to a lesser extent

441   with NDVI reflects the sensitivity of VV/VH, and particularly VH, to leaf emergence and

442   expansion. Leaf area development and growth act both in terms of number and geometrical

443   properties of scattering elements composed of leaves and young twigs, changes in their

444   dielectric properties especially through leaf water content and by masking the contribution of

445   trunks, branches, and soil. It is very likely that this last factor is the most important because

446 trees of the Fontainebleau-Barbeau forest are about 150 years old and the contribution of the

447 woody parts is expected to play a major role in winter and to decrease as LAI increases during

448 the spring. During this phenological stage, foliage development and expansion also modulate

449 NDVI and LAI very strongly although they also depend on canopy structure and leaf structural

450 and biochemical characteristics. During the senescence phase, the onset of VV/VH decline,

451 estimated from the SOF criterion, is later than for NDVI and LAI and practically synchronous

452 with litterfall. NDVI decreases before leaf fall due to leaf yellowing and browning that

453 characterize autumn leaf senescence. During this period, in addition to the decrease in leaf

454 chlorophyll content which is the main cause of the decrease in NDVI, leaf water content and

455 leaf mass also decreased as shown in previous studies (Yang et al., 2016; Yang et al., 2017;

456 Meerdink et al. ,2016). LAI, calculated in this study from transmitted radiation, also decreases

457 earlier, probably due to an increase of canopy transmissivity caused by a decrease in leaf

458 chlorophyll content during this period. Therefore, VV/VH seems to depend much more on the

459 amount of scattering elements (leaves, twigs, branches and trucks) which is better described by

460 litterfall than by NDVI or LAI.

461 While for various types of crops, many studies have shown a positive relationship between

462 VH backscatter coefficient in C-band and LAI or NDVI (Mandal et al., 2019; Wang et al.,

463 2019), our results show that, in deciduous forests, these relationships are inverted. Temporal

464 dynamics of LAI and NDVI is accompanied by a decrease in VH and an increase of VV/VH

465 ratio. These relationships are also not unique but depend on the phenological stage considered.

466 The use of S-1 signal in classifications or in fusion with optical remote sensing or its

467 interpretation should be considered with great care.

468 **5**. **Conclusion**

469 Time-series of Sentinel-1 A and B backscattering coefficients were used to characterize the

470 seasonal phenological cycles in a temperate deciduous forest over five years. While the

471 backscattering coefficient in vertical polarization (σ^0VV) remains relatively stable over the

472 seasons, the backscattering coefficient in cross-polarization (σ^0VH) responds significantly to

473 the seasonal vegetation cycle, with a behavior that is opposite to what is usually observed on

474   various crops. σ^0VH decreases during spring simultaneously with spring budburst and leaf

475   expansion, reaches a minimum during the main growing season when canopy leaf area is at its

476   maximum and increases again simultaneously with leaf fall. The observed σ^0VH seasonal

477   amplitude is 1.8 dB on average. S-1 time series of VV/VH ratio provides a good description of

478   the seasonal vegetation cycle, allowing the extraction of spring and autumn phenological

479   markers. Estimates of budburst dates in spring differ by approximately 8 days on average from

480   field phenological observations. During the senescence phase, the estimates provided by

481   VV/VH are late by about 20 days in comparison to field phenological observations and deviate

482   significantly by about two to four weeks from the estimates provided by *in situ* NDVI, S2-based

483   NDVI and LAI time-series. While during the spring, temporal pattern of VV/VH correlates

484   well with LAI and NDVI, during senescence, it is better explained by the dynamics of litterfall.

485   The deviation between VV/VH and litterfall-based senescence estimates is reduced to about

486   one week. A hysteresis phenomenon is observed on the relationships between VV/VH and

487   NDVI or LAI. For the same LAI or NDVI, the response of VV/VH is lower during canopy

488   foliage increase in spring than during leaf senescence and fall in autumn. These relationships

489   are not unique and lead to the conclusion that the mechanisms involved in the seasonality of

490   VV/VH signal are different according to the phenological stage considered. This behavior can

491   be explained by the preponderant contribution of woody parts in VH polarization

492   backscattering, which decreases as the forest canopy becomes more and more closed during

493   spring and summer and increases again during leaf senescence and fall in autumn. The

494   hysteresis phenomenon shows that attenuation of σ^0VH signal by canopy foliage appears to be

495   less important during spring and early summer than during senescence. This may be caused by

496   two opposing mechanisms: a significant role of water content of canopy foliage during the

497   spring which has the effect of causing an increase of σ^0VH and the role of foliage, which masks

498   the woody components, and has an opposite effect of causing a decrease in σ^0VH. This last

499   mechanism appears to be preponderant since σ^0VH decreases during the spring transition as

500   shown in this study but also in previous studies. During the senescence, the strong relationship

501   between the σ^0VH increase and the opening of the canopy caused by litterfall suggests that the

502 masking role played by foliage is also dominant. These results show that the interpretation of

503 S-1 signals over deciduous forest canopies or their use for classification without or after fusion

504 with optical data must be carried out with great care due to the temporal variability of the

505 contributions of the different canopy components associated with the seasonal phenological

506 cycle. The use of physical approaches based on radar backscatter models in forest canopies will

507 have the advantage of allowing a better understanding and evaluation of the contributions of the

508 different ecosystem components in the measured signal. It will also provide useful information

509 to better establish the correspondence between indirect phenological metrics predicted from the

510 S-1 time series and field phenological observations.

511

512 **References**

513 Benninga, H.J.F., van der Velde, R., Su, Z., 2019. Impacts of Radiometric Uncertainty and

514 Weather-Related Surface Conditions on Soil Moisture Retrievals with Sentinel-1. Remote

515 Sens. 2019, 11, 2025.

516 Bolton, D.K., Gray, J.M., Melaas, E.K., Moon, M., Eklundh, L., Friedl, M.A., 2020.

517 Continental-scale land surface phenology from harmonized Landsat 8 and Sentinel-2 imagery.

518 Remote Sens. Environ. 2020, 240, 111685.

519 Delpierre, N., Berveiller, D., Granda, E., Dufrêne, E., 2016. Wood phenology, not carbon

520 input, controls the interannual variability of wood growth in a temperate oak forest. New

521 Phytol. 210, 459-470.

522 Delpierre, N., Soudani, K., Berveiller, D., Dufrêne, E., Hmimina, G., Vincent, G., 2020.

523 "Green pointillism": detecting the within-population variability of budburst in temperate

524 deciduous trees with phenological cameras. Int. J. Biometeorol. 64, 663-670.

525 Denéchère, R., Delpierre, N., Apostol, E., Berveiller, D., Bonne, F., Cole, E., Delzon, S.,

526 Dufrêne, E., Gressler, E. Jean, F., Lebourgeois, F., Liu, G., Louvet, J., Parmentier, J., Soudani,

527 K., Vincent, G., 2019. The within-population variability of leaf spring and autumn phenology is

528 influenced by temperature in temperate deciduous trees. Int. J. Biometeorol. 2019.

529 Dostálová, A., Milenkovic, M., Hollaus, M., Wagner, W., 2016. Influence of forest

530 structure on the Sentinel-1 backscatter variation—Analysis with full-waveform lidar data.

531 Proceedings of the ESA Living Planet Symposium, Prague, Czech Republic, 9–13 May 2016.

532   Dostálová, A., Wagner, W., Milenković, M., Hollaus, M., 2018. Annual seasonality in

533   Sentinel-1 signal for forest mapping and forest type classification. Int. J. Remote Sens., 1 –23.

534   El Hajj, M., Baghdadi, N., Zribi, M., Angelliaume, S., 2016. Analysis of Sentinel-1

535   Radiometric Stability and Quality for Land Surface Applications. Remote Sens. 2016, 8, 406.

536   ESA   –   European   Space   Agency   Website:

537   https://sentinel.esa.int/web/sentinel/user-guides/sentinel-1-sar/revisit-and-coverage.

538   Fisher, J.I., Mustard, J.F, Vadeboncoeur, M.A., 2006. Green leaf phenology at Landsat

539   resolution: Scaling from the field to the satellite. Remote Sens. Environ. 100, 265–79.

540   Frison, P.-L., Fruneau, B., Kmiha, S., Soudani, K., Dufrêne, E., Le Toan, T., Koleck, T.,

541   Villard, L., Mougin, E., Rudant, J.-P., 2018. Potential of Sentinel-1 Data for Monitoring

542   Temperate Mixed Forest Phenology. Remote Sens. 2018, 10, 2049.

543   Gielen, B., Acosta, M., Altimir, N. et al., 2018. Ancillary vegetation measurements at

544   ICOS ecosystem stations. Int. Agrophys. 10, 645–664.

545   Hird, J.N., McDermid, G.J., 2009. Noise reduction of NDVI time series: An empirical

546   comparison of selected techniques. Remote Sens. Environ. 113, 248–258.

547   Hmimina, G., Dufrene, E., Pontailler, J.- Y., Delpierre, N., Aubinet, M., Caquet, B., de

548   Grandcourt, A., Burban, B., Flechard, C., Granier, A., Gross, P., Heinesch, B., Longdoz, B.,

549   Moureaux, C., Ourcival, J.-M., Rambal, S., Saint-André, L., Soudani, K., 2013. Evaluation of

550   the potential of MODIS satellite data to predict vegetation phenology in different biomes: An

551   investigation using ground based NDVI measurements. Remote Sens. Environ. 132, 145–158.

552   Jong, J. D., Klaassen, W., Ballast, A., 2000. Rain storage in forests detected with ERS

553   tandem mission SAR. Remote Sens. Environ. 72, 170–180

554   Khabbazan, S., Vermunt, P., Steele-Dunne, S., Ratering Arntz, L., Marinetti, C., van der

555   Valk, D., Iannini, L., Molijn, R., Westerdijk, K., van der Sande, C. 2019. Crop Monitoring

556   Using Sentinel-1 Data: A Case Study from The Netherlands. Remote Sens. 2019, 11, 1887.

557   Klosterman, S.T., Hufkens, K., Gray, J.M., Melaas, E., Sonnentag, O., Lavine, I., Mitchell,

558   L., Norman, R., Friedl, M.A., Richardson, A.D., 2014. Evaluating remote sensing of deciduous

559   forest phenology at multiple spatial scales using PhenoCam imagery. Biogeosciences Discuss.

560   11 (16), 4305–4320.

561   Kowalski, K., Senf, C., Hostert, P., Pflugmacher, D., 2020. Characterizing spring

562   phenology of temperate broadleaf forests using Landsat and Sentinel-2 time series. Int. J. Appl.

563   Earth Obs. 92, 102172.

564   Lange, M., Dechant, B., Rebmann, C., Vohland, M., Cuntz, M., Doktor, D., 2017.
565   Validating MODIS and Sentinel-2 NDVI Products at a Temperate Deciduous Forest Site Using
566   Two Independent Ground-Based Sensors. Sensors 17, 1855.

567   Mandal, D., Hosseini, M., McNairn, H., Kumar, V., Bhattacharya, A., Rao, Y.S., Mitchell,
568   S., Robertson, D.L., Davidson, A., Dabrowska-Zielinska K., 2019. An investigation of
569   inversion methodologies to retrieve the leaf area index of corn from C-band SAR data. Int. J.
570   Appl. Earth Obs. 82, 2019, 101893..

571   Meerdink, S.K, Roberts, D.A., King, J.Y., Roth, K.L., Dennison, P.E., Amaral, C.H.,
572   Hook, S.J., 2016. Linking seasonal foliar traits to VSWIR-TIR spectroscopy across California
573   ecosystems, Remote Sens. Environ. 186, 322–338.

574   Ose, K., Corpetti, T., Demagistri, L., 2016. Multispectral Satellite Image Processing.
575   In N. Baghdadi & M. Zribi (Eds.), Optical remote sensing of land surface techniques and
576   methods. Elsevier, 2016, pp 57–124.

577   Proisy, C., Mougin, E., Dufrêne, E., Le Dantec, V.,2000. Monitoring seasonal changes of a
578   mixed temperate forest using ERS SAR observations. IEEE T. Geosci. Remote Sens., 38,
579   540–552.

580   Reed, B.R, White, M.A., Brown, J.F., 2003. Remote sensing phenology. In Phenology: An
581   Integrative Environmental Science (ed. Schwartz M.D), Kluwer Academic Publishers, pp.
582   365–381.

583   Richardson, A.D., Black, T.A., Ciais, P., Delbart, N., Friedl, M.A., Gobron, N., Hollinger,
584   D.Y., Kutsch, W.L., Longdoz, B., Luyssaert, S., Migliavacca, M., Montagnani, L., Munger,
585   J.W., Moors, E., Piao, S., Rebmann, C., Reichstein, M., Saigusa, N., Tomelleri, E., Vargas, R.,
586   Varlagin, A., 2010. Influence of spring and autumn phenological transitions on forest
587   ecosystem productivity. Philos. Trans. R. Soc. Lond., B, Biol. Sci., 365,3227–3246.

588   Rüetschi, M., Schaepman, E. M., Small, D., 2018. Using Multitemporal Sentinel-1 C-band
589   Backscatter to Monitor Phenology and Classify Deciduous and Coniferous Forests in Northern
590   Switzerland. Remote Sens. 2018, 10.

591   Schaber, J., Badeck, F.W., 2002. Evaluation of methods for the combination of
592   phenological time series and outlier detection. Tree Physiol. 22, 973–982.

593   Song, Y., Wang, J., 2019. Mapping Winter Wheat Planting Area and Monitoring Its
594   Phenology Using Sentinel-1 Backscatter Time Series. Remote Sens. 2019, 11, 449.

595   Soudani, K., Delpierre, N., Berveiller, D., Hmimina, G., Pontailler, J.-Y., Seureau, L.,
596   Vincent, G., Dufrêne, E. ,2020. A survey of proximal methods for monitoring leaf phenology in
597   temperate deciduous forests, Biogeosciences Discuss., doi.org/10.5194/bg-2020-389, in
598   review, 2020.

599   Soudani, K., le Maire, G., Dufrêne, E., François, C., Delpierre, N., Ulrich, E., Cecchini, S.,
600   2008. Evaluation of the onset of green-up in temperate deciduous broadleaf forests derived
601   from Moderate Resolution Imaging Spectroradiometer (MODIS) data. Remote Sens. Environ.
602   12, 2643–2655.

603   Soudani, K., Hmimina, G., Delpierre, N., Pontailler, J.-Y., Aubinet, M., Bonal, D., Caquet,
604   B., de Grandcourt, A., Burban, B., Flechard, C., Guyon, D., Granier, A., Gross, P., Heinesh, B.,
605   Longdoz, B., Loustau, D., Moureaux, C., Ourcival, J.-M., Rambal, S., Saint André, L., Dufrêne,
606   E., 2012. Ground-based Network of NDVI measurements for tracking temporal dynamics of
607   canopy structure and vegetation phenology in different biomes. Remote Sens. Environ. 123,
608   234–245.

609   Stendardi, L., Karlsen, S.R., Niedrist, G., Gerdol, R., Zebisch, M., Rossi, M., Notarnicola,
610   C., 2019. Exploiting Time Series of Sentinel-1 and Sentinel-2 Imagery to Detect Meadow
611   Phenology in Mountain Regions. Remote Sens. 2019, 11, 542.

612   Sudmanns, M., Tiede D., Augustin, H., Lang, S., 2019. Assessing global Sentinel-2
613   coverage dynamics and data availability for operational Earth observation (EO) applications
614   using the EO-Compass. Int. J. Digit. Earth 1–17.

615   Vavlas, N.-C., Waine, T.W., Meersmans, J., Burgess, P.J., Fontanelli, G., Richter, G.M.,
616   2020. Deriving Wheat Crop Productivity Indicators Using Sentinel-1 Time Series. Remote
617   Sens. 2020, 12, 2385.

618   Veloso, A, Mermoz, S., Bouvet, A, Le Toan, T, Planells, M, Dejoux, J-F, Ceschia, E.,
619   2017. Understanding the temporal behavior of crops using Sentinel-1 and Sentinel-2-like data
620   for agricultural applications, Remote Sens. Environ. 199, 2017, 415–426.

621   Vreugdenhil, M., Wagner, W., Bauer-Marschallinger, B., Pfeil, I., Teubner, I., Rüdiger, C.,
622   Strauss, P., 2018. Sensitivity of Sentinel-1 Backscatter to Vegetation Dynamics: An Austrian
623   Case Study. Remote Sens. 2018, 10, 1396.

624   Vrieling, A., Meroni M., Darvishzadeh, R., Skidmore, A.K., Wang T., Zurita-Milla, R.,
625   Oosterbeek, K., O'Connor B., Paganini, M., 2018. Vegetation phenology from Sentinel-2 and
626   field cameras for a Dutch barrier island. Remote Sens. Environ. 2018, 215, 517–529.

627   Yang, X, Tang J, Mustard, JF., Wu J., Zhao K., Serbin S. Lee J.E., 2016. Seasonal

628   variability of multiple leaf traits captured by leaf spectroscopy at two temperate deciduous

629   forests. Remote Sens. Environ., 179, 1–12.

630   Yang, H., Yang, X., Heskel, M., Sun, S., Tang, J., 2017.Seasonal variations of leaf and

631   canopy properties tracked by ground-based NDVI imagery in a temperate forest. Sci Rep. 2017,

632   7(1):1267.

633   Wang, J., Xiao, X., Bajgain, R., Starks, P., Steiner, J., Doughty, R.B., Chang, Q., 2019.

634   Estimating leaf area index and aboveground biomass of grazing pastures using Sentinel-1,

635   Sentinel-2 and Landsat images. ISPRS J. Photogramm. Remote Sens. 154, 189–201.

636   Wang, Q., Atkinson, P.M., 2018. Spatio-temporal fusion for daily Sentinel-2 images.

637   Remote Sens. Environ. 204, 31–42.

638   White, J.C, Wulder, M.A. 2013. The Landsat observation record of Canada: 1972-2012.
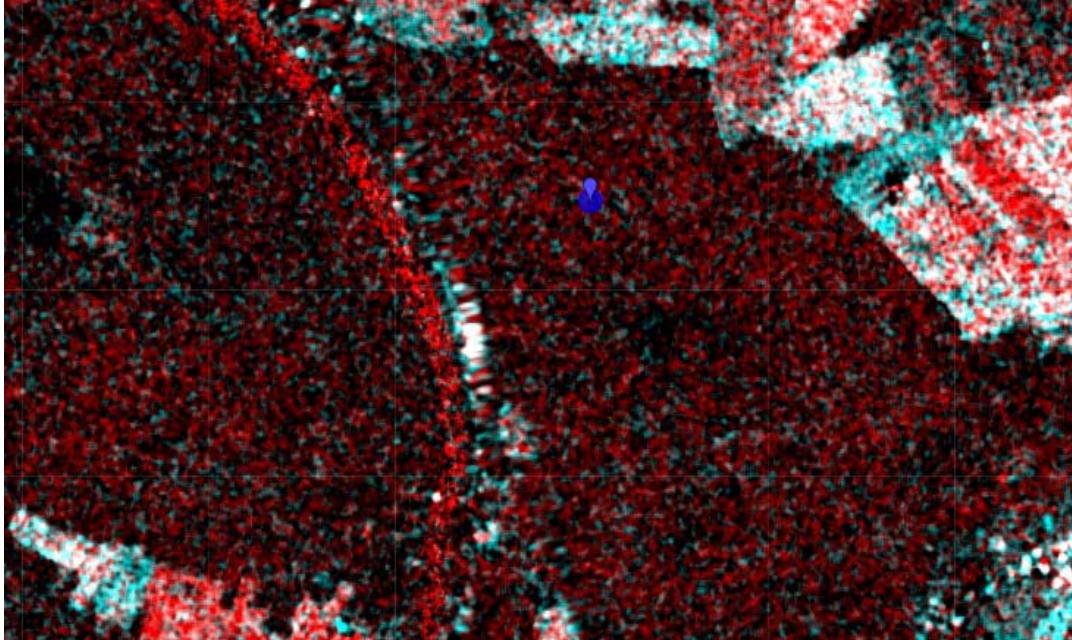
639   Can. J. Remote Sensing, 39, 6, 455–467.

640

641

642

Supplementary Materials

644

Figure S1: Fontainebleau-Barbeau forest location in France (48°28'26"N, 2°46'57"E). The blue circle with a radius of 50 m is centered on Fontainebleau-Barbeau flux tower (FR-Fon, ICOS network). The image is a Sentinel-1 RGB composite where average VV/VH during the summer (15/06/2018 - 31/08 2018) in red, average VV/VH during the winter (01/01 – 28/02 2018) in green and blue.
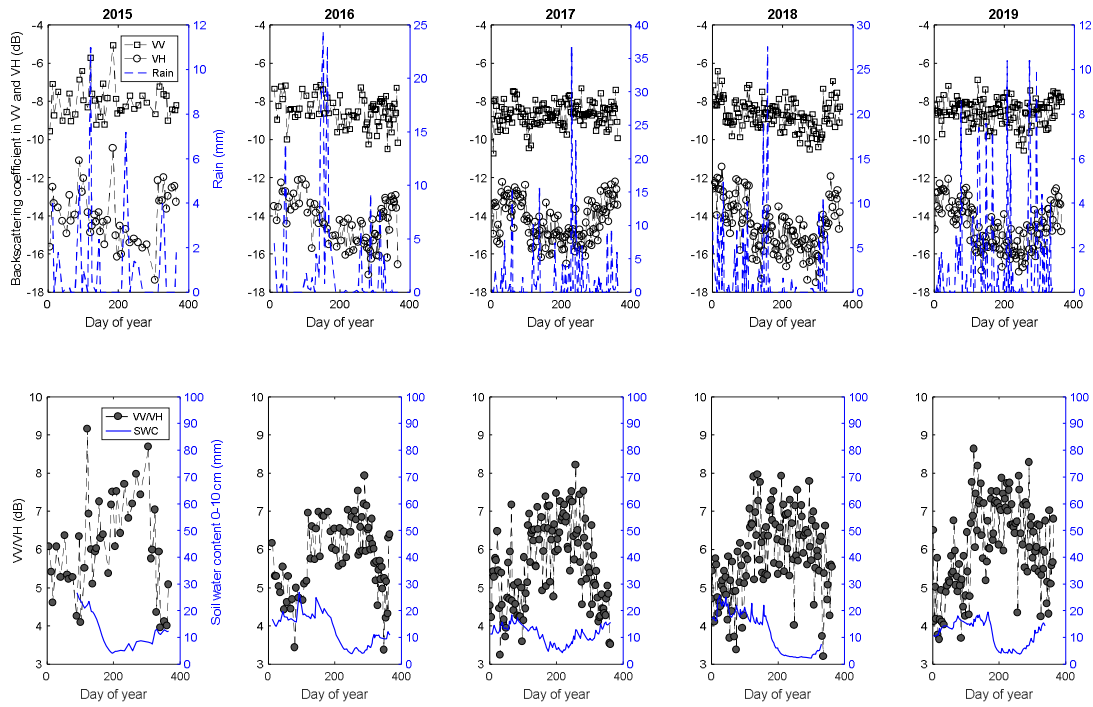
650

651
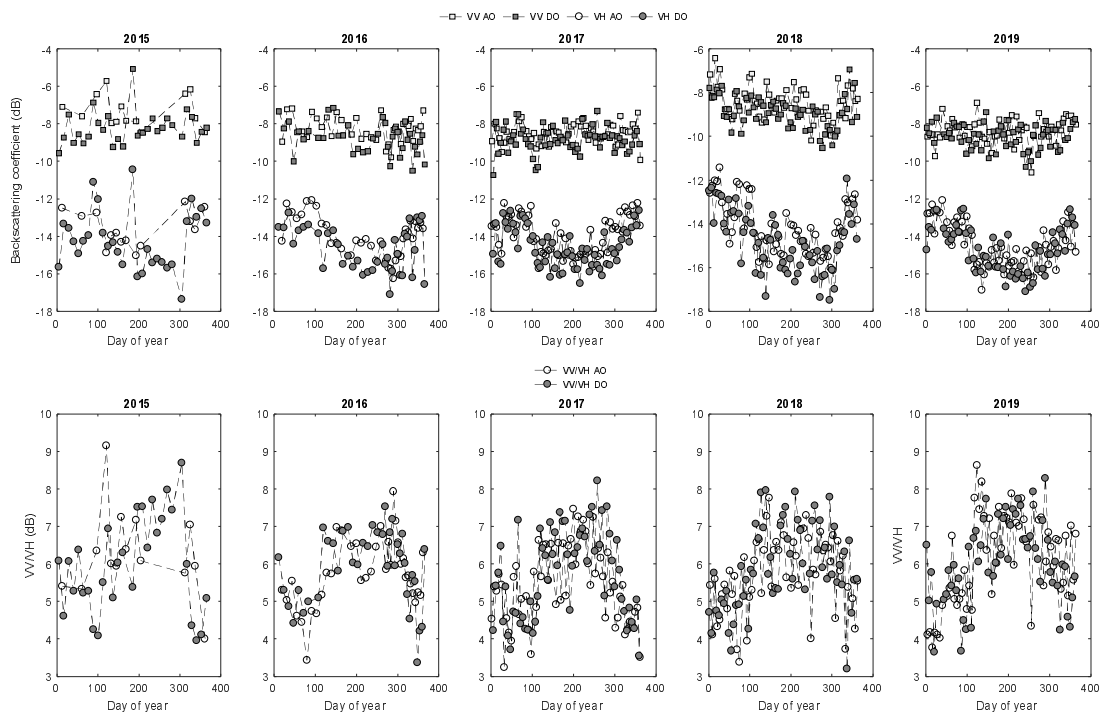
652

653 Figure S2: SAR backscattering coefficients σ^0 in VV and VH polarizations and VV/VH ratio
654 time-series from Sentinel-1 A&B. circle: VH polarization, square: VV polarization. Empty
655 (circles and squares) in ascending orbit and filled in descending orbit.

656

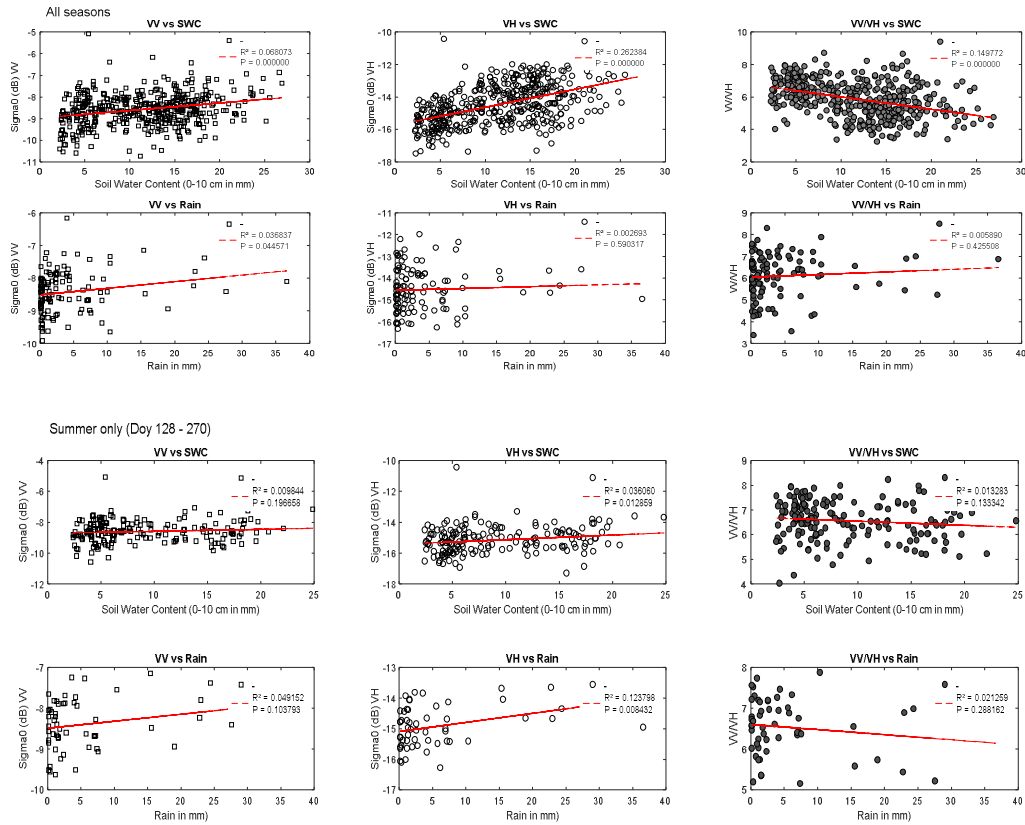Figure S3: Sentinel-1 σ^0VV (square symbol), σ^0VH (circle symbol) and VV/VH (filled circle) time-series over 2015-2019 period (right axis). In blue (left axis), rain (upper panel) and soil water content (0-10 cm) in mm (lower panel).

662

663   Figure S4: Linear regressions between Sentinel-1 data and soil water content (0-10 cm depth)
664   and rain during the year (all seasons – upper panel) and during summer season (lower panel).
665

666 Table S5: observed and estimated dates of onset of greenness in spring and leaf senescence and
667 fall based on field phenological observations and time-series of Sentinel-1 VV/VH,
668 ground-based normalized difference vegetation index (NDVI), Leaf area index (LAI), Litterfall
669 and Sentinel-2 NDVI.

	Budburst and leaf expansion			Leaf senescence and fall		
	SOS	MOS	EOS	SOE	MOE	EOE
Phenological observations						
2015	101	106	109	267	290	312
2016	102	109	115	282	300	317
2017	89	99	108	267	294	321
2018	-	105	-	-	-	-
2019	-	109	-	-	-	-
Sentinel-1 VV/VH						
2015	110	113	113	312	323	332
2016	100	123	144	304	321	336
2017	100	117	130	273	297	318
2018	89	104	115	292	323	350
2019	99	111	121	252	321	388
In situ NDVI						
2015	102	107	112	272	293	314
2016	103	113	123	280	302	324
2017	90	101	111	255	293	332
2018	100	106	112	272	311	349
2019	96	108	119	273	306	339
Leaf Area Index						
2015	100	113	124	251	287	322
2016	103	120	137	263	296	329
2017	90	111	131	248	288	327
2018	102	111	119	231	287	341
2019	98	115	131	250	292	334
Litter fall						
2015	-	-	-	266	301	309
2016	-	-	-	298	312	324
2017	-	-	-	273	300	322
2018	-	-	-	281	316	331
2019	-	-	-	288	317	329
S-2 NDVI						
2015						
2016	115	118	124	261	285	320
2017	105	113	121	303	316	328
2018	106	111	115	192	281	368
2019	83	99	114	253	296	337

670

671

672

673

674

675